Electronic Supplementary Material

Detailed mechanism and kinetics of the reaction of Criegee intermediate CH₂OO with HCOOH investigated via infrared identification of conformers of hydroperoxymethyl formate and formic acid anhydride

Chen-An Chung,[1] Jou Wei Su,[1] and Yuan-Pern Lee[1, 2, 3]*

[1]*Department of Applied Chemistry and Institute of Molecular Science, National Chiao Tung University, 1001, Ta-Hsueh road, Hsinchu 30010, Taiwan*

[2] *Center for Emergent Functional Matter Science, National Chiao Tung University, Hsinchu 30010, Taiwan.*

[3]*Institute of Atomic and Molecular Science, Academia Sinica, Taipei 10617, Taiwan*

*E-mail: yplee@nctu.edu.tw

A. Computational results

Geometries of possible intermediates in reaction $CH_2OO + HCOOH$ are shown in Fig. S3. Harmonic and anharmonic vibrational wavenumbers and harmonic IR intensities of conformers P1 and P2 of hydroxylated secondary ozonide (HSOZ) and conformers P4−P6 of hydroperoxymethyl formate (HPMF) predicted with the B3LYP/aug-cc-pVTZ method are listed in Tables S1 and S2, respectively. Those of *syn-* and *anti-*FAN (formic acid anhydride) predicted with the B3LYP/aug-cc-pVTZ method are listed in Table S3.

B. Estimate of the ratio of $V_{IR}/V_{photolysis}$

Because photolysis volume $V_{photolysis}$ is distinct from the IR-probe volume V_{IR}, we estimated the volume ratio to relate the IR absorption of CH_2OO with the true concentration of CH_2OO in the photolysis volume. The concentration c of each precursor can be estimated from its IR absorption according to the following equation:

$$c = \frac{\int A(v)\,dv \times ln(10)}{S_{band} \times L} \qquad (1)$$

in which $A(v)$ is the absorbance (base 10), $\int A(v)dv$ is the integrated intensity, S_{band} is the band intensity, and L is the IR absorption length, 367 cm.

To simulate properly the reaction kinetics of $CH_2OO + HCOOH$, we must know the initial concentration of CH_2OO or CH_2I in the reactor. Because the self-reaction of CH_2OO has been well characterized,[1,2,3,4] we found that we could estimate $[CH_2I]_0$, hence $[CH_2OO]_0$, on fitting the temporal profiles of $[CH_2OO]$ (integrated over region 905−915 cm^{-1}) in the photolysis experiments of CH_2I_2 and O_2 using the reported kinetic model and rate coefficients discussed in Sec. C; the reaction $CH_2OO + HCOOH$ was excluded from the model because no HCOOH was added in these experiments. Some representative temporal profiles of CH_2OO with their model fitted profiles (lines) are shown in Fig. S1; the satisfactory fits for the rise and decay of CH_2OO indicate that the model is adequate. From these fits, we derived $[CH_2I]_0$

in the photolysis volume. We derived $[CH_2I]_0$ in the IR-probe volume on probing the decrease in IR absorbance of CH_2I_2 upon photolysis according to eq. (1). The band intensity S_{band} for CH_2I_2 (in region 1090−1135 cm^{-1}) is 13.08×10^{-18} cm molecule^{-1} (Ref. 5). We then derived ratio $V_{IR}/V_{photolysis}$ according to $[CH_2I]_0$ in the IR-probe volume and the photolysis volume. Several experiments at varied pressure were performed. The resultant ratios $V_{IR}/V_{photolysis}$ are presented in Fig. S2; the average value is 2.65±0.24.

C. High-resolution spectra from CH_2I_2/HCOOH/N_2/O_2 (0.162/0.120/44.5/65.1, P_T = 109.9 Torr)

Observed spectra in region 850−1450 cm^{-1} upon photolysis of a mixture of CH_2I_2/HCOOH/N_2/O_2 (0.162/0.120/44.5/65.1, P_T = 109.9 Torr) recorded with an external ADC at resolution 0.5 cm^{-1} are presented in Fig. S4. Those in region 1600−1900 cm^{-1} at resolution 1 cm^{-1} are presented in Fig. S5.

D. Simulation of bands of HPMF

With program PGopher,[6] we simulated the fundamental band of each vibrational mode of isomers P5 and P6 of HPMF using rotational parameters A'', B'', and C'', ratios of rotational parameters A'/A'', B'/B'', and C'/C'' (Table S4) and a-type/b-type ratios (Table S5) of each mode predicted with the B3LYP/aug-cc-pVTZ-pp method, J_{max} = 200, T = 298 K, and Gaussian width 0.64 cm^{-1} (corresponding to the instrument resolution of 0.5 cm^{-1}).

Simulated a-, b-, and c-type spectra and the resultant spectra for bands A$_4$ (ν_{12}) and A$_5$ (ν_{11}) of HPMF (P5) are shown in Fig. S6. The squares of the projections of the dipole derivatives for each vibrational mode of HPMF onto rotational axes a, b and c determine the weighting of bands of types a, b, and c in each resultant vibrational absorption band. Because information was lacking, we assumed that the rotational contours and IR intensities of hot bands were the same as of the fundamental band. The contours of the hot bands were consequently derived from the fundamental band with intensities scaled according to a

Boltzmann distribution and positions shifted according to anharmonicity; the shifts depend on the difference in transition wavenumber between the fundamental band and the hot bands. We calculated, as initial estimates, the Boltzmann distributions of the excited states of the low-energy modes according to the predicted anharmonic vibrational energies of the low-frequency modes ($\nu_{24} = 79$ cm^{-1}, $\nu_{23} = 123$ cm^{-1}, $\nu_{22} = 214$ cm^{-1}); the shifts among hot bands in a series were constant. A least-squares fit was performed on systematically varying the positions of the band origins (within ≤ 5 cm^{-1} of the predicted values) and intensities (within $\pm 10\%$) for each band to obtain the best fit.

A comparison of the fitted contour with the experiment for bands A_4 (ν_{12}) and A_5 (ν_{11}) is presented in Fig. S7(a), in which the experimental data are presented with open circles and the simulated spectrum is shown as a thick red solid line. Each simulated feature consists of the fundamental band and hot bands in three series involving absorption from the excited states of the two torsional modes of least energy and one low-frequency bending mode; the dominant series of hot bands is associated with the torsion of OC−OC (ν_{24}), another with the torsion of OO−CO. (ν_{23}), and a third with the COC bending mode (ν_{22}). The components of hot bands in each individual series for bands A_5 and A_4 are shown in Figs. S7(b) and S7(c), respectively, with the same color for each series. Detailed positions and relative intensities of these components for bands A_5 and A_4 are listed in Tables S6 and S7, respectively. This simulation is not unique and is presented only to explain why the observed bands are much broader than those simulated without contributions of hot bands.

E. Kinetic model to fit the reaction CH_2OO + $HCOOH$

CH_2OO was produced from the reaction CH_2I + O_2 upon irradiation at 248 nm with an excimer laser of a flowing mixture of CH_2I_2 and O_2 at 298 K. The initial concentration of CH_2I_2 in the cell, $[CH_2I_2]_0$, was determined on comparison of the integrated absorbance in region 1090−1135 cm^{-1} with the literature value of band strength, as described in Sec. A; it

also agrees with the values obtained on comparison with a calibration curve obtained on measurement of its IR absorption of CH_2I_2 at varied pressure in a static cell. The initial concentration of CH_2I in the IR-proved volume was estimated from $-\Delta[CH_2I_2]$ upon irradiation. The initial concentration of CH_2I in the photolysis volume, $[CH_2I]_0$, is estimated by $-(V_{IR}/V_{photolysis}) \times \Delta[CH_2I_2] = -2.65 \times \Delta[CH_2I_2]$; the value of $V_{IR}/V_{photolysis}$ was discussed in Sec. A. This value was compared with $[CH_2I_2]_0 \times y$, in which y is the fractional yield of photodissociation of CH_2I_2. The value of y was obtained from $(F/h\nu_{308}) \times \sigma_{308}$, in which F is the laser fluence and σ_{308} is the absorption cross section of CH_2I_2 at 308 nm, 3.2×10^{-18} cm^2 molecule^{-1}.[7] Values of $[CH_2I]_0$ derived from both methods are consistent, but we employed those derived from $-\Delta[CH_2I_2]$ because they are derived spectroscopically. The concentration of HCOOH was determined from its integrated absorbance (in region 1050−1085 cm^{-1}) and the associated band intensity 5.83×10^{-18} cm molecule^{-1}.[8,9]

To measure rate coefficient k of the reaction CH_2OO + HCOOH, we employed a model slightly modified from that of our previous work,[2] as shown in Table S8. Following recent literature,[10] we separated the original channel (1c), $CH_2I + O_2 \rightarrow$ other products, into two channels, (1c) and (1d), with products CH_2O + IO and those from decomposition of CH_2OO, respectively. Traces in Fig. S8 show representative experimental temporal profiles of HPMF and curves fitted from the model under various conditions. Traces in Fig. S9 show representative experimental temporal profiles of CH_2OO and curves fitted from the model under various conditions. A summary of experimental conditions and the fitted results (k^I) of 32 measurements are shown in Table S9. A plot of first-order rate coefficient vs [HCOOH] is shown in Fig. 8 in the main text. The fitted bimolecular rate coefficient of each set of experiments is summarized in Table S10; the rate coefficient derived from fitting all data is k_1 = $(1.44 \pm 0.04) \times 10^{-10}$ cm^3 molecule^{-1} s^{-1}; the listed error represents one standard deviation in

the fit.

Considering the errors in the estimation of $[CH_2I]_0$ (~20 %), fitting error (12.8 %), error resulted from the uncertainties in rate coefficient of the self-reaction of CH_2OO (k_{self} in Table S8, the error of 25% transforms into an error of 1 % in k_1) and other standard errors in measurements of flow rates (1 %), temperature (1 %), and pressure (3 %), we estimated the overall uncertainty to be 24 %. A rate coefficient for the reaction of $CH_2OO + HCOOH$ at 298 K is hence reported to be $k_1 = (1.4\pm0.3)\times10^{-10}$ cm^3 molecule^{-1} s^{-1}.

F. Detailed mechanism of HPMF → FAN

To prove that the revised two-channel model discussed in the main text, Sec. 4.4 is valid, we compared temporal profiles of HPMF on integrating regions 1330−1370 cm^{-1} (which corresponds to a mixture of isomers P5 and P6 of HPMF) and 1157−1186 cm^{-1} (which corresponds to mostly P6 of HPMF), respectively, as shown in Fig. S10.

Table S1 Harmonic and anharmonic vibrational wavenumbers (cm^{-1}) and harmonic IR intensities (km mol^{-1}) of conformers P1 and P2 of hydroxylated secondary ozonide (HSOZ) predicted with the B3LYP/aug-cc-pVTZ method

Mode	P1		P2	
	Harmonic	Anharmonic	Harmonic	Anharmonic
ν_1	3778 (47)	3582	3801 (54)	3612
ν_2	3114 (3)	2970	3112 (10)	2961
ν_3	3111 (21)	2967	3044 (32)	2914
ν_4	3017 (64)	2794	3013 (70)	2806
ν_5	1520 (1)	1425	1521 (0)	1437
ν_6	1433 (71)	1391	1422 (267)	1385
ν_7	1399 (10)	1369	1394 (11)	1361
ν_8	1309 (4)	1273	1328 (35)	1300
ν_9	1286 (12)	1251	1247 (39)	1217
ν_{10}	1230 (3)	1199	1225 (3)	1194
ν_{11}	1156 (29)	1135	1148 (14)	1128
ν_{12}	1127 (391)	1095	1110 (451)	1077
ν_{13}	1075 (103)	1043	1079 (66)	1053
ν_{14}	1003 (92)	969	1026 (55)	998
ν_{15}	949 (72)	925	966 (62)	945
ν_{16}	889 (9)	861	914 (9)	890
ν_{17}	867 (18)	848	870 (15)	852
ν_{18}	790 (25)	775	815 (4)	799
ν_{19}	732 (2)	719	730 (4)	717
ν_{20}	555 (17)	542	566 (13)	555
ν_{21}	508 (19)	469	486 (7)	477
ν_{22}	337 (20)	280	304 (37)	213
ν_{23}	294 (68)	163	284 (86)	117
ν_{24}	130 (3)	134	128 (13)	124

Table S2 Harmonic and anharmonic vibrational wavenumbers (cm^{-1}) and harmonic IR intensities (km mol^{-1}) of conformers P4−P6 of hydroperoxymethyl formate (HPMF) predicted with the B3LYP/aug-cc-pVTZ method

Mode	P4		P5		P6	
	Harmonic	Anharmonic	Harmonic	Anharmonic	Harmonic	Anharmonic
ν_1	3748 (56)	3564	3740 (43)	3538	3511 (260)	3304
ν_2	3126 (6)	2985	3131 (6)	2983	3148 (3)	2998
ν_3	3038 (33)	2885	3067 (9)	2978	3076 (16)	2973
ν_4	2984 (38)	2853	3038 (48)	2889	3057 (42)	2902
ν_5	1838 (395)	1801	1784 (323)	1751	1760 (281)	1727
ν_6	1485 (4)	1464	1479 (7)	1458	1497 (88)	1435
ν_7	1425 (11)	1394	1410 (33)	1385	1470 (6)	1444
ν_8	1401 (15)	1370	1398 (4)	1364	1419 (5)	1385
ν_9	1384 (38)	1352	1381 (41)	1346	1403 (4)	1369
ν_{10}	1314 (19)	1279	1284 (1)	1256	1306 (10)	1275
ν_{11}	1183 (176)	1155	1196 (301)	1157	1197 (269)	1147
ν_{12}	1091 (115)	1058	1138 (123)	1115	1150 (16)	1128
ν_{13}	1037 (63)	1014	1090 (79)	1060	1076 (102)	1044
ν_{14}	1031 (111)	1002	1040 (0)	1020	1049 (6)	1026
ν_{15}	1019 (141)	992	929 (109)	901	899 (7)	876
ν_{16}	882 (31)	861	885 (38)	860	829 (130)	799
ν_{17}	693 (23)	681	780 (1)	768	781 (12)	768
ν_{18}	533 (6)	523	545 (2)	537	606 (115)	510
ν_{19}	424 (5)	416	407 (28)	395	542 (6)	535
ν_{20}	337 (9)	325	320 (50)	250	438 (6)	428
ν_{21}	272 (93)	189	270 (97)	255	302 (19)	291
ν_{22}	186 (25)	162	222 (4)	214	245 (8)	218
ν_{23}	141 (36)	136	140 (5)	123	205 (9)	198
ν_{24}	79 (1)	79	29 (2)	79	104 (2)	95

Table S3 Harmonic and anharmonic vibrational wavenumbers (cm^{-1}) and harmonic IR intensities (km mol^{-1}) of *syn-* and *anti-*FAN (formic acid anhydride) predicted with the B3LYP/aug-cc-pVTZ method

Mode	*syn-*FAN		*anti-*FAN	
	Harmonic	Anharmonic	Harmonic	Anharmonic
ν_1	3049 (35)	2897	3089 (9)	2939
ν_2	3047 (46)	2897	3058 (32)	2902
ν_3	1882 (322)	1844	1860 (157)	1832
ν_4	1795 (188)	1763	1809 (443)	1781
ν_5	1409 (2)	1375	1406 (4)	1374
ν_6	1393 (2)	1359	1381 (2)	1353
ν_7	1081 (696)	1041	1104 (609)	1065
ν_8	1045 (0)	1024	1046 (0)	1025
ν_9	1007 (111)	993	1034 (0)	1018
ν_{10}	972 (4)	952	1005 (242)	971
ν_{11}	797 (34)	781	781 (6)	766
ν_{12}	561 (14)	555	538 (6)	532
ν_{13}	216 (26)	203	252 (10)	248
ν_{14}	211 (1)	208	224 (11)	217
ν_{15}	103 (2)	83	75 (39)	89

Table S4 Rotational parameters of the ground state and vibrationally excited states ($v = 1$) of conformers P5 and P6 of HPMF predicted with the B3LYP/aug-cc-pVTZ method

Mode	HPMF (P5)			HPMF (P6)		
	A'/A''	B'/B''	C'/C''	A'/A''	B'/B''	C'/C''
ν_1	1.002	1.000	0.999	0.999	0.999	1.000
ν_2	0.999	1.000	1.000	1.002	0.998	0.999
ν_3	1.001	1.000	0.999	1.004	0.990	0.995
ν_4	0.996	1.000	1.000	1.000	0.999	1.000
ν_5	0.998	1.000	0.999	0.999	0.999	0.999
ν_6	1.000	1.000	1.001	1.000	1.000	0.999
ν_7	1.002	0.999	0.997	1.004	0.987	0.994
ν_8	1.000	1.001	1.000	0.999	0.999	0.998
ν_9	0.998	0.999	0.999	0.998	0.998	0.997
ν_{10}	0.996	1.000	1.001	0.998	0.999	0.999
ν_{11}	0.987	0.999	1.001	0.998	0.999	1.000
ν_{12}	1.020	0.997	0.992	0.997	0.997	0.998
ν_{13}	0.982	0.999	1.003	1.001	0.999	0.999
ν_{14}	0.999	0.999	0.999	0.998	0.998	0.998
ν_{15}	1.002	0.997	1.003	0.999	1.000	1.000
ν_{16}	0.997	0.998	0.998	1.002	0.999	1.000
ν_{17}	1.006	0.998	0.996	0.999	0.997	0.999
ν_{18}	1.003	0.997	0.998	1.000	1.003	1.001
ν_{19}	0.968	1.003	1.010	1.001	0.996	0.998
ν_{20}	1.022	0.996	0.992	0.998	1.001	0.999
ν_{21}	1.001	0.999	1.000	1.000	0.999	0.999
ν_{22}	1.005	0.998	0.998	0.999	1.000	1.000
ν_{23}	1.007	0.999	0.999	0.999	1.001	1.000
ν_{24}	0.991	1.000	1.005	0.995	1.011	1.004
	A'' / cm^{-1}	B'' / cm^{-1}	C'' / cm^{-1}	A'' / cm^{-1}	B'' / cm^{-1}	C'' / cm^{-1}
$v = 0$	0.4025	0.0603	0.0571	0.1949	0.1099	0.0750

Table S5 Ratios of *a*-, *b*-, and *c*-types of vibrational bands for each vibrational mode of conformers P5 and P6 of HPMF predicted with the B3LYP/aug-cc-pVTZ method

Mode	HPMF (P5)			HPMF (P6)		
	a-type	*b*-type	*c*-type	*a*-type	*b*-type	*c*-type
ν_1	0.11	0.80	0.09	0.91	0.09	0.00
ν_2	0.10	0.00	0.90	0.10	0.56	0.34
ν_3	0.01	0.79	0.20	0.01	0.51	0.48
ν_4	0.14	0.78	0.08	0.91	0.03	0.06
ν_5	0.65	0.25	0.10	0.01	0.99	0.00
ν_6	0.48	0.31	0.21	0.34	0.60	0.06
ν_7	0.83	0.15	0.02	0.26	0.04	0.70
ν_8	0.48	0.52	0.00	0.46	0.31	0.23
ν_9	0.32	0.40	0.28	0.01	0.98	0.01
ν_{10}	0.03	0.00	0.97	0.27	0.70	0.03
ν_{11}	0.97	0.03	0.00	0.51	0.47	0.02
ν_{12}	0.87	0.04	0.09	0.56	0.01	0.43
ν_{13}	0.97	0.00	0.03	0.95	0.00	0.05
ν_{14}	0.89	0.11	0.00	0.93	0.05	0.02
ν_{15}	0.46	0.49	0.05	0.11	0.46	0.43
ν_{16}	0.98	0.02	0.00	0.98	0.00	0.02
ν_{17}	0.96	0.04	0.00	0.75	0.12	0.13
ν_{18}	0.93	0.01	0.06	0.15	0.18	0.67
ν_{19}	0.49	0.02	0.49	0.43	0.08	0.49
ν_{20}	0.37	0.08	0.55	0.05	0.12	0.83
ν_{21}	0.88	0.01	0.11	0.56	0.13	0.31
ν_{22}	0.46	0.30	0.24	0.79	0.19	0.02
ν_{23}	0.92	0.06	0.02	0.13	0.87	0.00
ν_{24}	0.01	0.13	0.86	0.46	0.49	0.05

Table S6 Relative population of the lower state and band origins of hot bands employed in the simulation of the ν_{11} band of HPMF (P5)

Transition	Relative population	Band origins / cm^{-1}
11_0^1	1.00	1169.5
$11_0^1 24_1^1$	0.85	1176.5
$11_0^1 24_2^2$	0.58	1185.5
$11_0^1 24_3^3$	0.40	1191.5
$11_0^1 24_4^4$	0.13	1201.8
$11_0^1 24_5^5$	0.05	1210.0
$11_0^1 24_6^6$	0.02	1218.0
$11_0^1 23_1^1$	0.67	1163.5
$11_0^1 23_2^2$	0.35	1153.5
$11_0^1 23_3^3$	0.21	1145.5
$11_0^1 23_4^4$	0.11	1141.0
$11_0^1 23_5^5$	0.06	1134.0
$11_0^1 22_1^1$	0.42	1159.0
$11_0^1 22_2^2$	0.18	1141.0
$11_0^1 22_3^3$	0.05	1122.0

Table S7 Relative population of the lower state and band origins of hot bands employed in the simulation of the ν_{12} band of HPMF (P5)

Transition	Relative population	Band origins / cm^{-1}
12_0^1	1.00	1115.0
$12_0^1 24_1^1$	0.72	1110.5
$12_0^1 24_2^2$	0.45	1107.0
$12_0^1 24_3^3$	0.22	1103.0
$12_0^1 24_4^4$	0.10	1099.0
$12_0^1 24_5^5$	0.04	1095.0
$12_0^1 24_6^6$	0.01	1091.0
$12_0^1 23_1^1$	0.58	1121.0
$12_0^1 23_2^2$	0.32	1128.0
$12_0^1 23_3^3$	0.18	1133.0
$12_0^1 23_4^4$	0.10	1139.0
$12_0^1 23_5^5$	0.06	1145.0
$12_0^1 22_1^1$	0.37	1135.0
$12_0^1 22_2^2$	0.05	1155.0

Table S8 Kinetic model employed in fitting the temporal profiles of $CH_2OO + HCOOH$

	reaction	rate coefficient [a]	condition	reference
$k_{1a}{}^b$	$CH_2I + O_2 \rightarrow CH_2OO + I$	$1.5\times10^{-12}/(1+1.1\times10^{-19}\,[M])$	P≥60 Torr	2
β	Fraction of survival of CH_2OO		P<60 Torr	2
	when P<60 Torr,	$\{1- 0.47/(1+3.2\times10^{-18}\,[M])\}$		
	$\beta= k_{1a'}/k_{1a}$			
$k_{1b}{}^b$	$CH_2I + O_2 \rightarrow ICH_2OO$	$1.5\times10^{-12} - k_{1a}$	P≥60 Torr	2
$k_{1c}{}^b$	$CH_2I + O_2 \rightarrow other + I$	$k_{1a}(1-\beta) - k_{1d}$	P<60 Torr	2
$k_{1d}{}^b$	$CH_2I + O_2 \rightarrow H_2CO + IO$	4.0×10^{-13}	P<60 Torr	10
k_{2a}	$CH_2OO + I \rightarrow CH_2I + O_2$	$55k_{1a}$		2
k_{2b}	$CH_2OO + I \rightarrow ICH_2OO$	$55k_{1b}$		2
k_{2c}	$CH_2OO + I \rightarrow H_2CO + IO$	9.0×10^{-12}		2
k_3	$CH_2OO + CH_2I \rightarrow C_2H_4I + O_2$	6.3×10^{-11}		11
k_{self}	$2CH_2OO \rightarrow 2H_2CO + O_2$	8.0×10^{-11}		1−4
k_4	$ICH_2OO + I \rightarrow ICH_2O + IO$	3.5×10^{-11}		12
k_5	$2ICH_2OO \rightarrow 2ICH_2O + O_2$	9.0×10^{-11}		12
k_6	$ICH_2O \rightarrow H_2CO + I$	$10^6\ s^{-1}$		12
k_7	$2IO \rightarrow I_2 + O_2$	9.9×10^{-11}		13
k_8	$CH_2OO + HCOOH \rightarrow product$	$k^I = k_8\times[HCOOH]_0$, fitted		

[a] rate coefficient in cm^3 molecule^{-1} s^{-1}, unless specified otherwise, [M] in molecule cm^{-3}. [b] $k_{1a} + k_{1b} + k_{1c} + k_{1d} = 1.5\times10^{-12}$ cm^3 molecule^{-1} s^{-1}.

Table S9 First-order rate coefficients of reaction $CH_2OO + HCOOH$ in varied sets of experiments

Set	Expt.	region /cm^{-1}	$[CH_2I_2]_0$ /mTorr	$[CH_2I]_0$ /$10^{14\ a}$	$[CH_2OO]_0$ /$10^{14\ a}$	$[O_2]_0$ /Torr	$[N_2]_0$ /Torr	[HCOOH] /$10^{15\ a}$	k^I /10^5 s^{-1}
1	1	1157−1186	45	2.4	1.5	53	47	1.4	2.2
	2	1157−1186	45	2.4	1.5	53	47	1.7	2.6
	3	1157−1186	45	2.4	1.5	53	47	1.9	2.9
	4	1157−1186	45	2.4	1.5	53	47	2.2	3.6
	5	1157−1186	45	2.4	1.5	53	47	2.5	3.8
	6	1157−1186	45	2.4	1.5	53	47	3.0	4.3
	7	1157−1186	45	2.4	1.5	53	47	3.0	4.4
2	8	1157−1186	37	1.4	0.87	53	47	1.7	2.9
	9	1157−1186	37	1.4	0.87	53	47	2.0	3.2
	10	1157−1186	37	1.4	0.87	53	47	2.3	3.8
	11	1157−1186	37	1.4	0.87	53	47	2.5	4.2
	12	1157−1186	37	1.4	0.87	53	47	2.7	4.4
3	13	1157−1186	30	1.1	0.67	53	47	1.7	2.5
	14	1157−1186	30	1.1	0.67	53	47	2.0	3.0
	15	1157−1186	30	1.1	0.67	53	47	2.4	3.2
	16	1157−1186	30	1.1	0.67	53	47	2.6	3.8
	17	1157−1186	30	1.1	0.67	53	47	3.1	4.3
4	18	1157−1186	45	2.4	1.3	120	90	2.1	3.0
	19	1157−1186	45	2.4	1.3	120	90	2.3	3.3
	20	1157−1186	45	2.4	1.3	120	90	2.5	3.6
	21	1157−1186	45	2.4	1.3	120	90	2.7	3.8
	22	1157−1186	45	2.4	1.3	120	90	2.8	3.8
	23	1157−1186	45	2.4	1.3	120	90	2.9	4.0
	24	1157−1186	45	2.4	1.3	120	90	3.1	4.3
5	25	1157−1186	18	1.3	1.0	20	0	0.58	0.65
	26	1157−1186	18	1.3	1.0	20	0	1.0	1.1
	27	1157−1186	18	1.3	1.0	20	0	2.1	2.6
	28	1157−1186	18	1.3	1.0	20	0	2.5	3.1
6	29	1000−1050	42	2.9	2.1	40	0	1.5	1.9
	30	1000−1050	42	2.9	2.1	40	0	2.9	4.3
	31	1000−1050	42	2.9	2.1	40	0	3.6	5.0
	32	1000−1050	42	2.9	2.1	40	0	5.0	7.2

[a] in unit of molecule cm^{-3}.

Table S10 Bimolecular rate coefficients of the reaction $CH_2OO + HCOOH$ in six sets of experiments.

Set	P_{total} /Torr	k_1 /10^{-10} cm^3 molecule^{-1} s^{-1}
1	110	1.35
2	110	1.38
3	110	1.27
4	210	1.50
5	20	1.30
6	40	1.50
average of 6 sets		1.38±0.09
all data		1.44±0.04
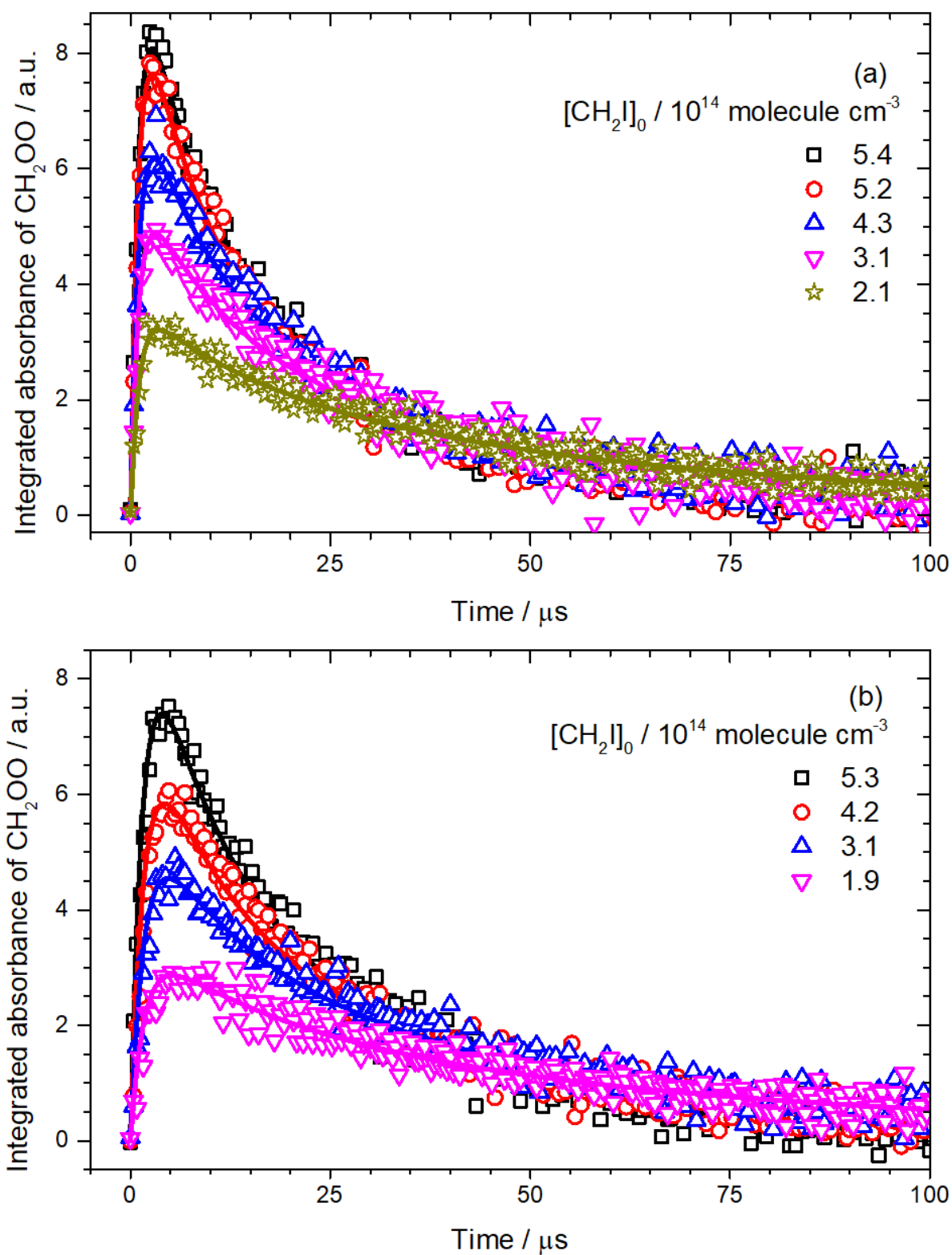
Fig. S1 Representative temporal profiles of CH$_2$OO in experiments of irradiated CH$_2$I$_2$/O$_2$ and model fitting. (a) O$_2$ = 12 Torr and CH$_2$I$_2$ = 0.05−0.14 Torr, (b). O$_2$ = 20 Torr and CH$_2$I$_2$ = 0.06−0.18 Torr. Integrated area 905−915 cm^{-1}.
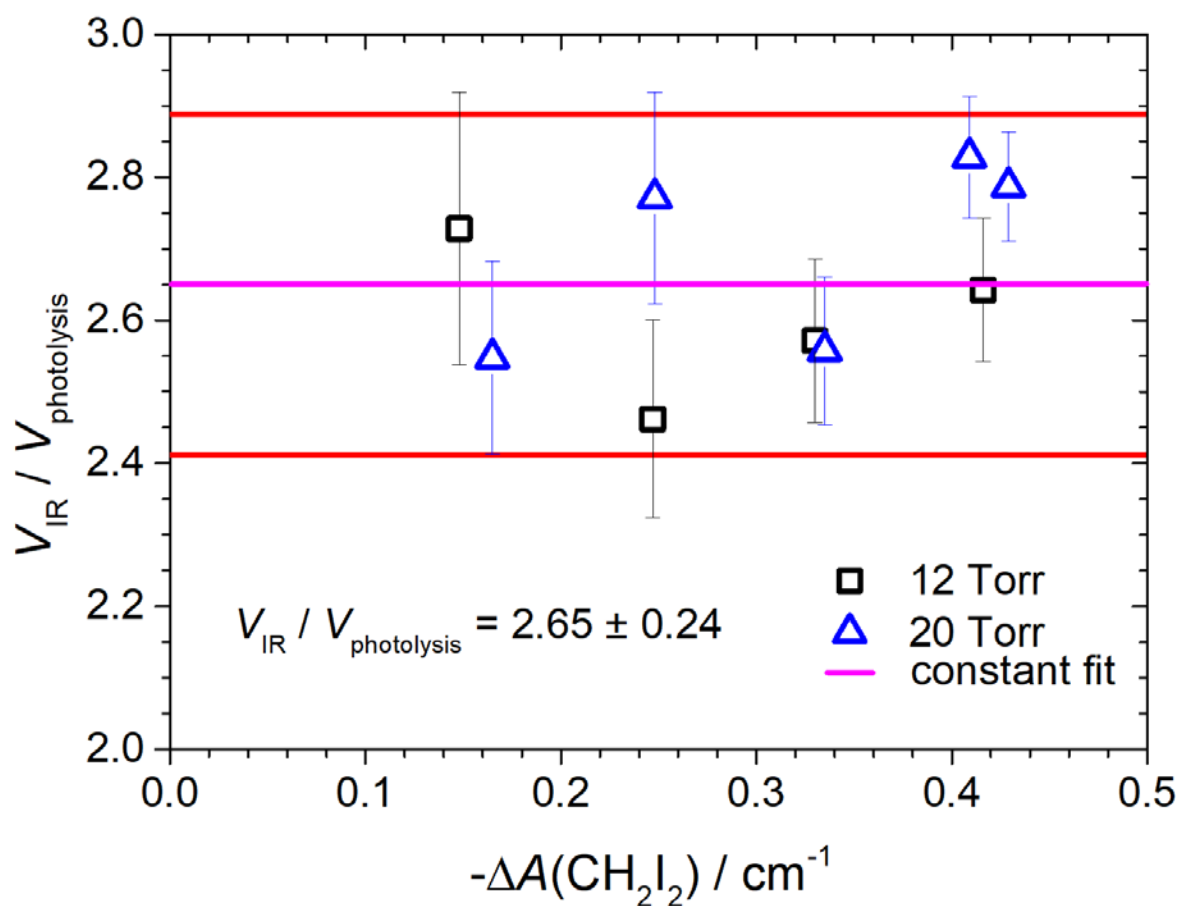
Fig. S2 Measurements of ratios $V_{IR}/V_{photolysis}$ at varied integrated absorpbance change of CH_2I_2 upon irradiation at 248 nm. Integrated spectral range is 1090−1035 cm^{-1}. The red lines represent one standard deviation of the fit.
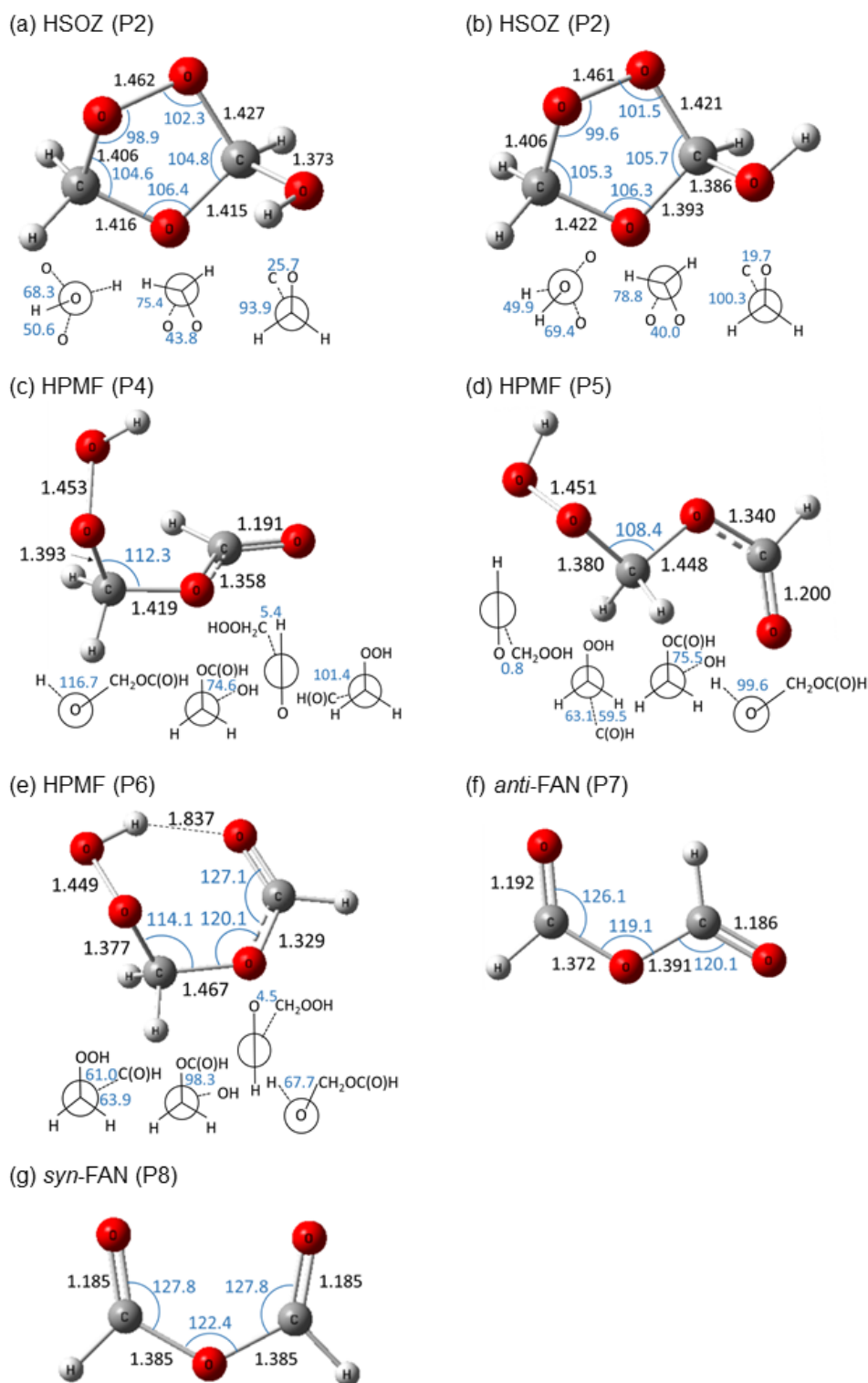
Fig. S3 Geometries of possible intermediates in reaction $CH_2OO + HCOOH$. The notations of the species in Long *et al*. [*J. Mol. Struct. THEOCHEM*, 2009, **916**, 159−167] are listed in parentheses. (a) HSOZ (P1), (b) HSOZ (P2), (c) HPMF (P4), (d) HPMF (P5), (e) HPMF (P6), (f) *anti*-FAN (P7), and (g) *syn*-FAN (P8) predicted with the B3LYP/aug-cc-pVTZ method. The bond distances are given in Å and the bond angles in degree.
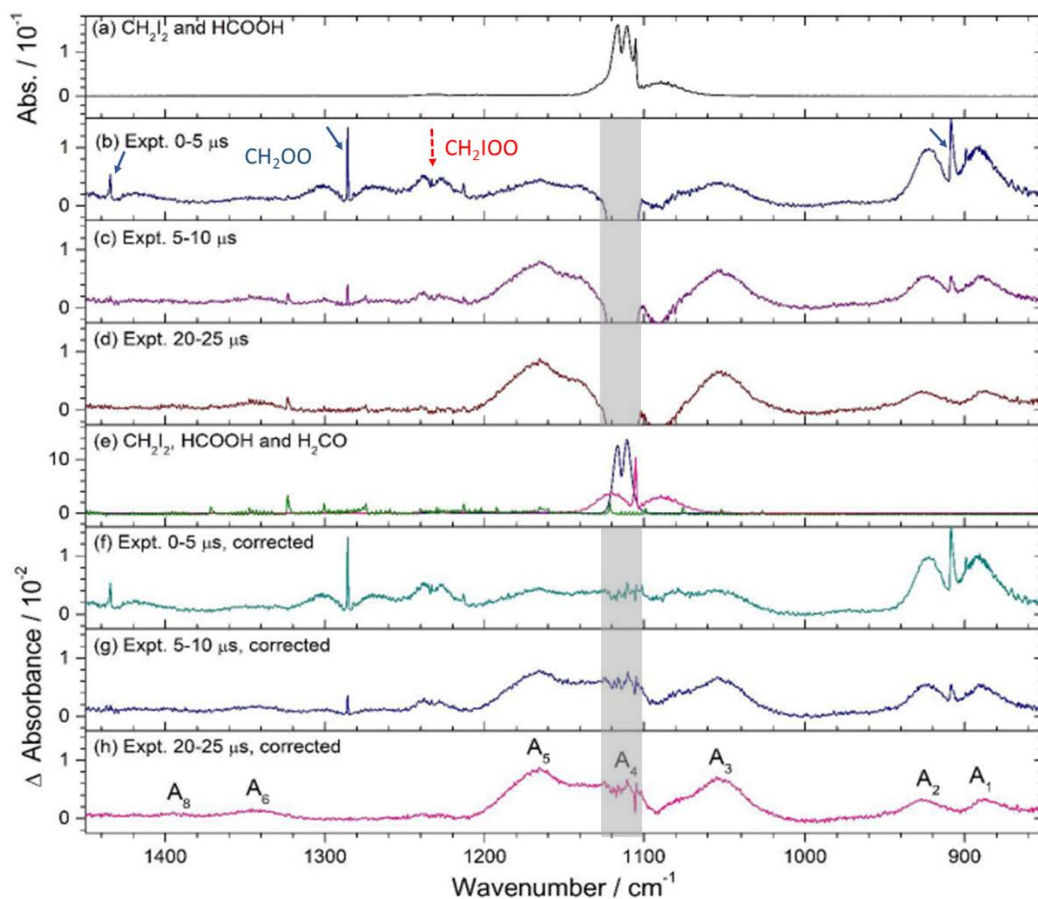
Fig. S4 Observed spectra in region 850−1450 cm^{-1} upon photolysis of a mixture of CH$_2$I$_2$/HCOOH/N$_2$/O$_2$ (0.162/0.120/44.5/65.1, P_T = 109.9 Torr) recorded with an external ADC. (a) Spectrum before photolysis. Difference spectra recorded 0−5 μs (b), 5−10 μs (c), and 20−25 μs (d) after irradiation of the sample at 308 nm. Resolution is 0.5 cm^{-1}. (e) Reference spectra of CH$_2$I$_2$ (black), HCOOH (red), and H$_2$CO (green). Spectra with CH$_2$I$_2$, HCOOH, and H$_2$CO removed are shown for 0−5 μs (f), 5−10 μs (g), and 20−25 μs (h). Absorption bands of CH$_2$OO and CH$_2$IOO are indicated with blue and red arrows, respectively, in (b). The region with severe interference from CH$_2$I$_2$ is indicated with grey rectangular background.
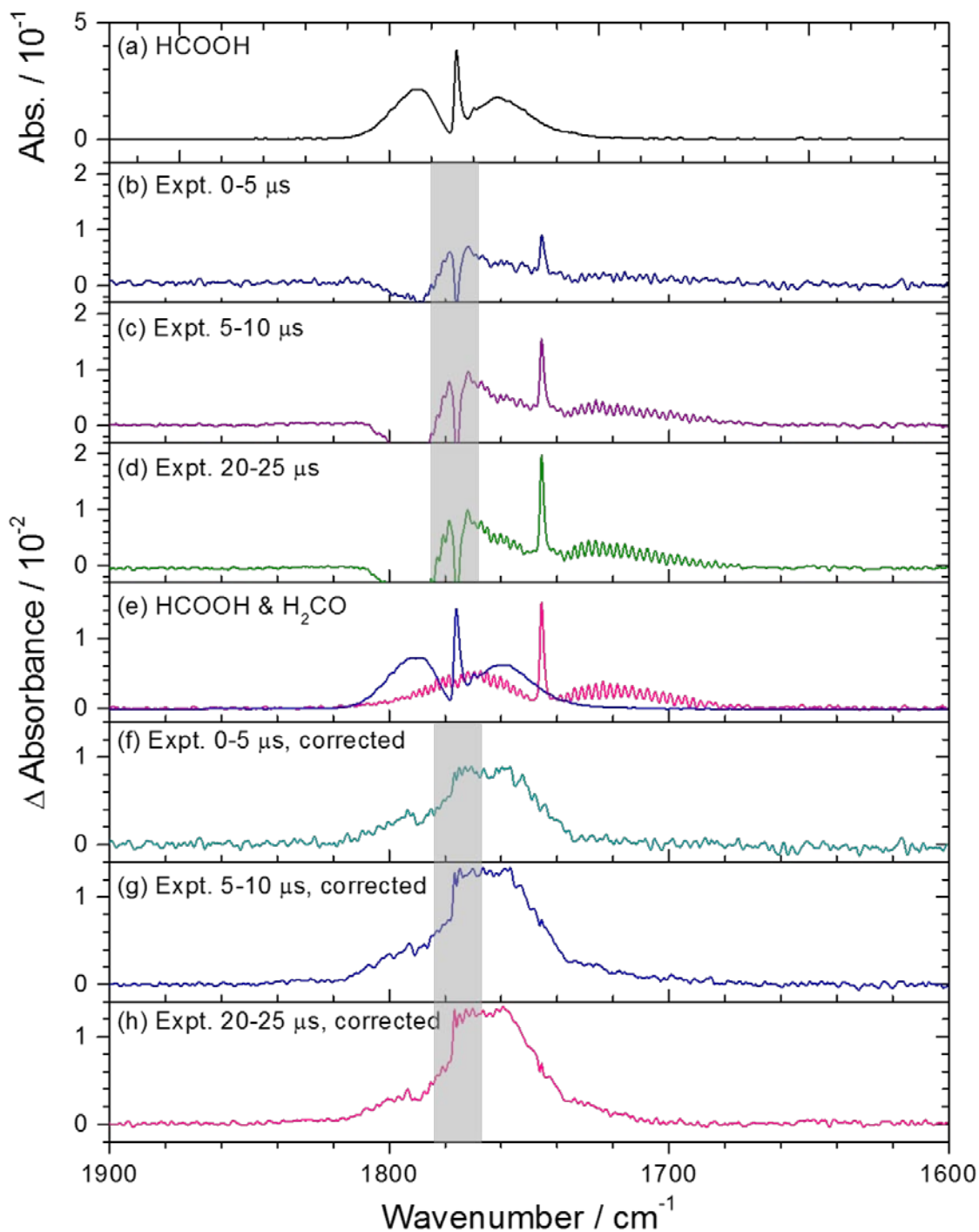
Fig. S5 Temporal evolution of observed spectra in region 1600−1900 cm^{-1} upon photolysis of a mixture of CH$_2$I$_2$/HCOOH/N$_2$/O$_2$ (0.162/0.120/44.5/65.1, P_T = 109.9 Torr) recorded with an external ADC. **(a)** Spectrum before photolysis. Difference spectra recorded 0−5 µs (b), 5−10 µs (c), and 20−25 µs (d) after irradiation of the sample at 308 nm. Resolution is 1 cm^{-1}. (e) Reference spectra of HCOOH (blue), and H$_2$CO (red). Spectra with HCOOH and H$_2$CO removed are shown for 0−5 µs (f), 5−10 µs (g), and 20−25 µs (h). The region with severe interference from HCOOH is indicated with grey rectangular background.
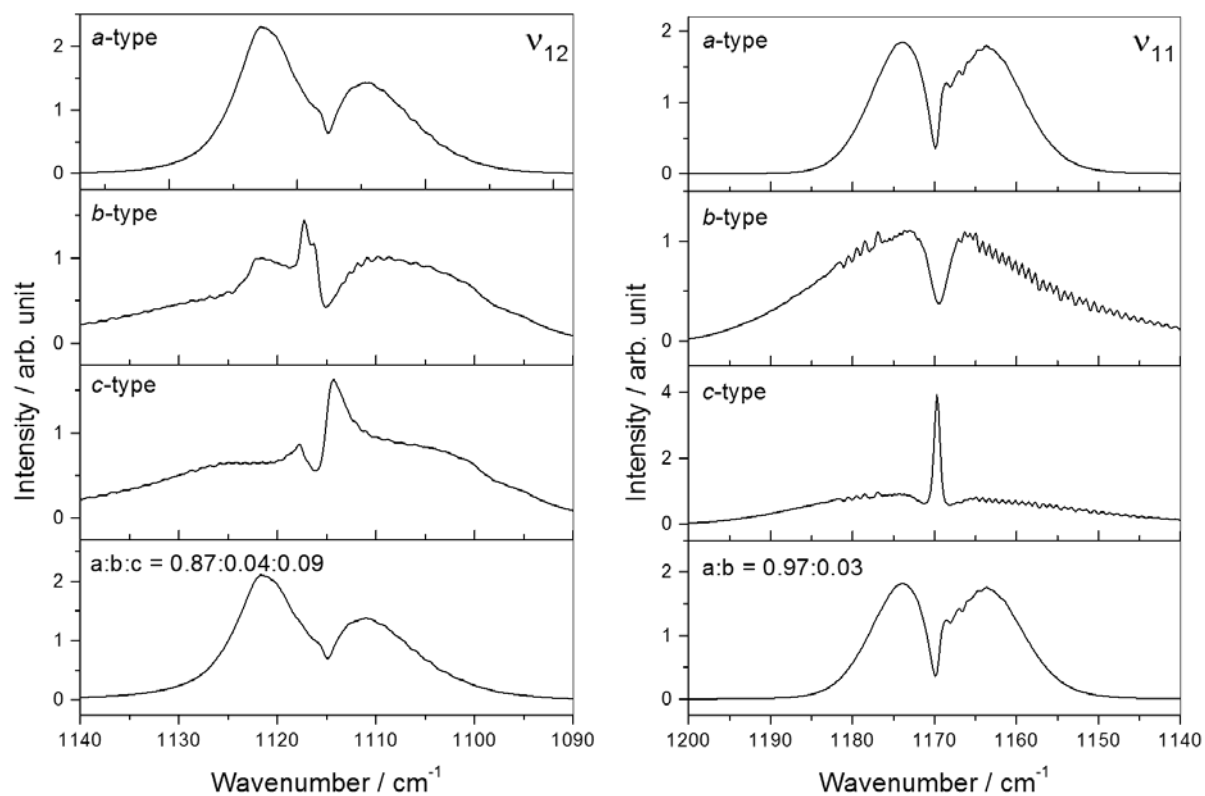
Fig. S6 Simulated *a*-, *b*-, and *c*-type spectra and the resultant spectra for bands A$_4$ (ν_{12}) and A$_5$ (ν_{11}) of HPMF (P5).
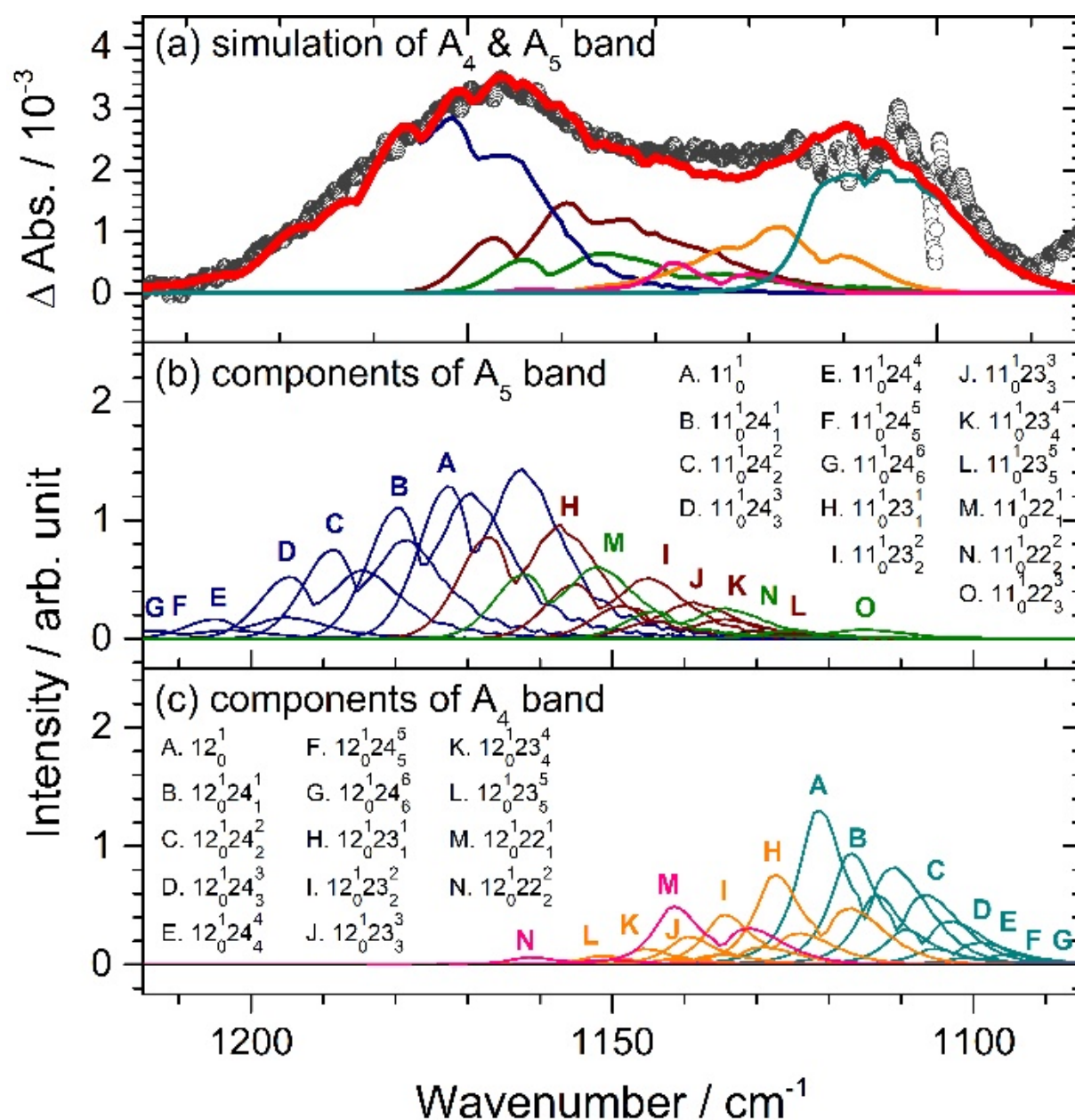
(a) simulation of A_4 & A_5 band

Δ Abs. / 10^{-3}

(b) components of A_5 band

Intensity / arb. unit

A. 11_0^1
B. $11_0^1 24_1^1$
C. $11_0^1 24_2^2$
D. $11_0^1 24_3^3$
E. $11_0^1 24_4^4$
F. $11_0^1 24_5^5$
G. $11_0^1 24_6^6$
H. $11_0^1 23_1^1$
I. $11_0^1 23_2^2$
J. $11_0^1 23_3^3$
K. $11_0^1 23_4^4$
L. $11_0^1 23_5^5$
M. $11_0^1 22_1^1$
N. $11_0^1 22_2^2$
O. $11_0^1 22_3^3$

(c) components of A_4 band

A. 12_0^1
B. $12_0^1 24_1^1$
C. $12_0^1 24_2^2$
D. $12_0^1 24_3^3$
E. $12_0^1 24_4^4$
F. $12_0^1 24_5^5$
G. $12_0^1 24_6^6$
H. $12_0^1 23_1^1$
I. $12_0^1 23_2^2$
J. $12_0^1 23_3^3$
K. $12_0^1 23_4^4$
L. $12_0^1 23_5^5$
M. $12_0^1 22_1^1$
N. $12_0^1 22_2^2$

Wavenumber / cm^{-1}

1200   1150   1100

Fig. S7 Comparison of the fitted contour with experiment for bands A_4 (ν_{12}) and A_5 (ν_{11}). (a) Experimental data (open circle) and simulated results (thick line: total; thin lines: fundamental and each series of hot bands). (b) The components of each individual series of hot bands for band A_5. (c) The components of each individual series of hot bands for band A_4.
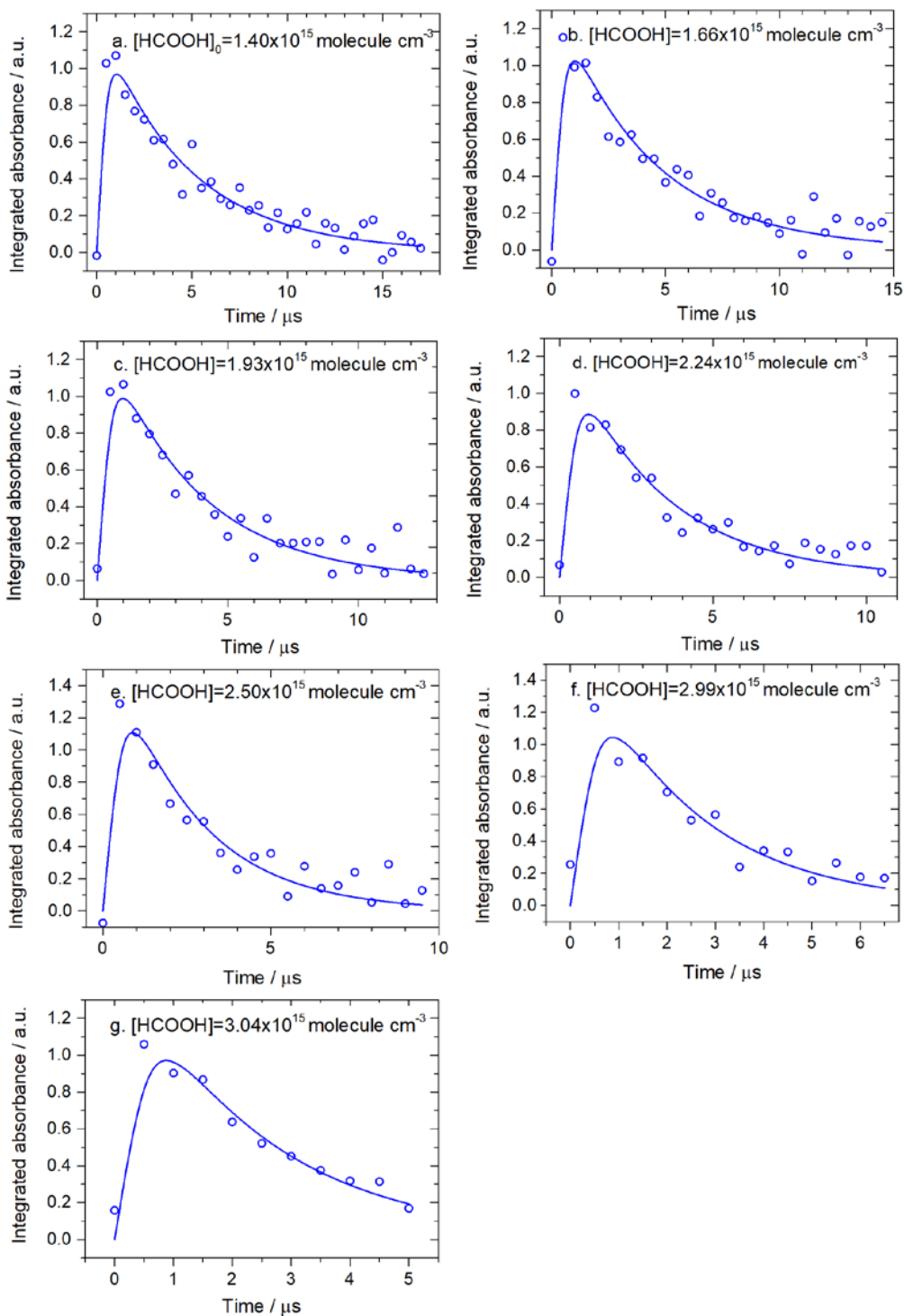
Fig. S8 Representative experimental results and fitted temporal profiles for the decay of
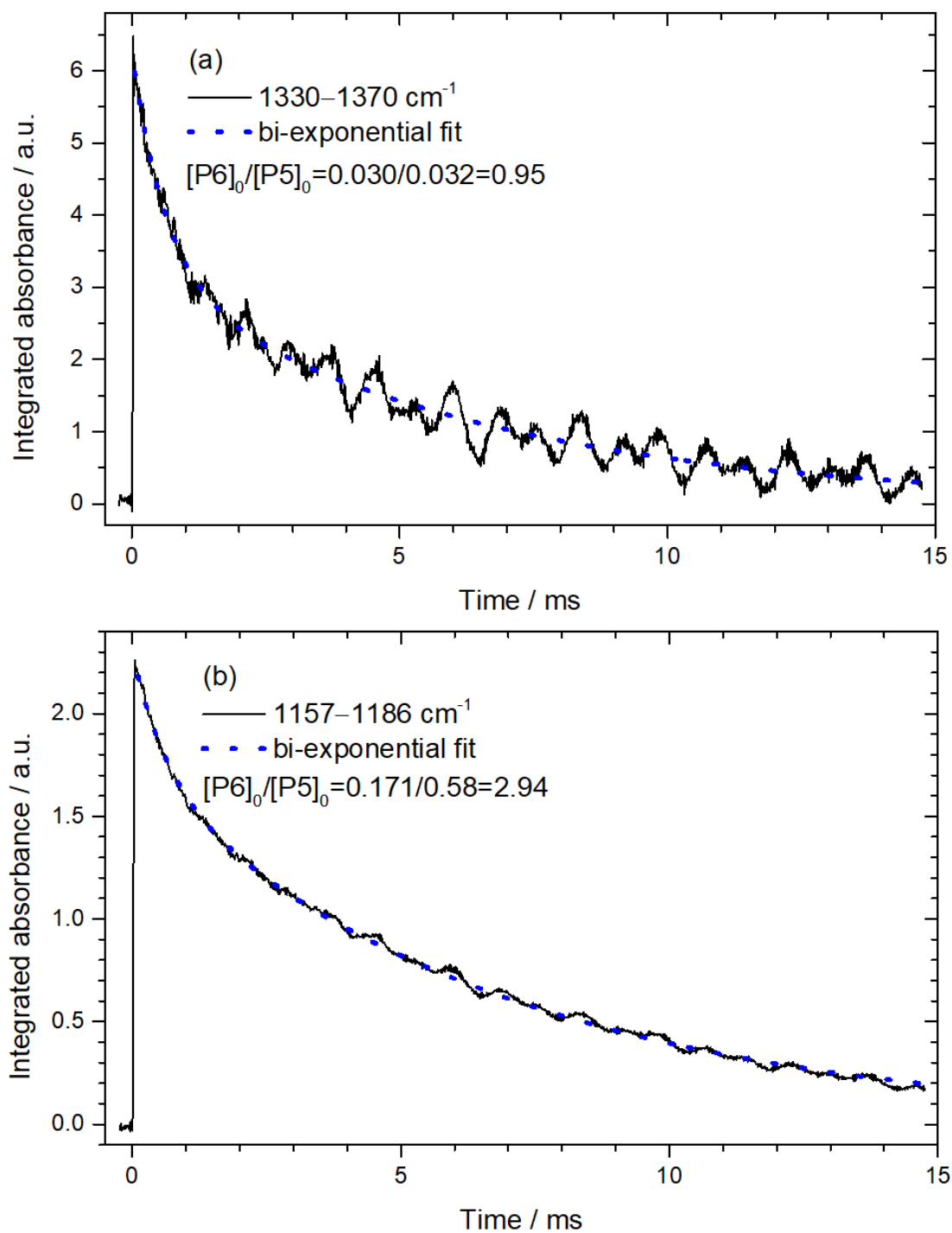
CH$_2$OO at different [HCOOH]$_0$ for data set one.

Fig. S9 Comparison of decay profiles of HPMF obtained from integration in varied regions. (a) 1330−1370 cm^{-1} (b) 1157−1186 cm^{-1}

References

[1] Z. J. Buras, R. M. I. Elasmra and W. H. Green, *J. Phys. Chem. Lett.*, 2014, **5**, 2224−2228

[2] W.-L. Ting, C.-H. Chang, Y.-F. Lee, H. Matsui, Y.-P. Lee and J. J.-M. Lin, *J. Chem. Phys.*, **141**, 104308 (2014).

[3] P.-L. Luo, Y. Endo and Y.-P. Lee, *J. Phys. Chem. Lett*., 2018, **9**, 4391−4395.

[4] R. Chhantyal-pun, A. Davey, D. E. Shallcross, C. J. Percival and A. J. Orr-Ewing, *Phys. Chem. Chem. Phys.*, 2015, **17**, 3617−3626.

[5] T. J. Johnson, T. Masiello and S. W. Sharpe, *Atmos. Chem. Phys.*, 2006, **6**, 2581−2591.

[6] C. M. Western, *PGOPHER, a Program for Simulating Rotational Structure*, http://pgopher.chm.bris.ac.uk/.

[7] C. Mössinger, D. E. Shallcross and R. A. Cox, *J. Chem. Soc. Faraday Trans.*, 1998, **94**, 1391−1396.

[8] A. Perrin and J. V. Auwera, *J. Quant. Spectrosc. Radiat. Trans.*, 2007, 108, 363−370.

[9] J. V. Auwera, K. Didriche, A. Perrin and F. Keller, *J. Chem. Phys.*, 2007, **126**, 124311.

[10] S. Enami, J. Ueda, M. Goto, Y. Nakano, S. Aloisio, S. Hashimoto and M. Kawasaki, J. Phys. Chem. A, 2004, 108, 6347−6350.

[11] Y.-T. Su, H.-Y. Lin, R. Putikam, H. Matsui, M. C. Lin and Y.-P. Lee, *Nat. Chem.*, 2014, **6**, 477−483.

[12] T. J. Gravestock, M. A. Blitz, W. J. Bloss and D. E. Heard, *ChemPhysChem*, 2010, **11**, 3928−3941.

[13] R. Atkinson, D. L. Baulch, R. A. Cox, J. N. Crowley, R. F. Hampson, Jr., R. G. Hynes, M. E. Jenkin, M. J. Rossi and J. Troe, *Atmos. Chem. Phys.*, 2007, **7**, 981−1191.